Letter

Graphene bilayer and trilayer moiré lattice with Rashba spin-orbit coupling

Y. Avishai [1,2] and Y. B. Band [1,3]

[1] *Department of Physics, Ben-Gurion University of the Negev, Beer Sheva, Israel*

[2] *Yukawa Institute for Theoretical Physics, Kyoto, Japan*

[3] *Department of Chemistry, Department of Electro-Optics, and The Ilse Katz Center for Nano-Science, Ben-Gurion University of the Negev, Beer Sheva, Israel*

(Received 18 October 2021; revised 9 March 2022; accepted 11 July 2022; published 26 July 2022)

We study the behavior of equilibrium spin currents near the magic angles of twisted bilayer and trilayer graphene in the presence of Rashba spin-orbit coupling. There is a substantial difference in the properties of local observables in twisted graphene layers, as compared with those in single and/or untwisted graphene layers. Remarkably, when plotted as a function of the twist angle θ, the electronic charge density and the equilibrium spin currents are nonanalytic at angles that are close to within 1% of the magic angles. In addition to the occurrence of rich spin texture patterns, these findings enable the determination of magic angles within an accuracy of less than 0.01° in terms of a scanning tunneling microscopy measurement of the local density and spin-resolved measuring devices for measuring equilibrium spin currents.

DOI: 10.1103/PhysRevB.106.L041406

Introduction. Van Hove singularities in twisted bilayer graphene (TBG) and the emergence of flat bands at certain twisting angles were first reported in Refs. [1–3]. A continuous model for exploring the electronic structure of TBG that forms a moiré lattice was developed in Ref. [4] and exposed the occurrence of magic angles θ_{2m}, i.e., twist angles at which the lowest (positive) energy band is flat versus crystal momentum. Their origin was clarified in Refs. [5–7], while the symmetries and topological content of this system were analyzed in Refs. [8–10]. Recent reports have shown that this system can host correlated insulating states [11,12], unconventional superconductivity [13], distinct Landau level degeneracies [14], emergent ferromagnetism with an anomalous Hall effect and quantized anomalous Hall behavior [15–17], chirality [18], valley spirals [19], and optospintronics [20]. The flatness of the band is very sensitive to the value of the magic angle, hence, an accurate determination of the magic angle is crucial [21].

In the present Letter we consider TBG and twisted trilayer graphene (TTG) subject to a uniform perpendicular electric field that causes Rashba spin-orbit coupling (RSOC) [22], and substantiate the relevance of magic angles to the pertinent spin physics. The Bloch functions $\{\Psi_{\mathbf{k}}(\mathbf{r})\}$ of the lowest conduction band at crystal momentum $\mathbf{k}$ are calculated and employed to determine the charge density $\rho_{\mathbf{k}}(\mathbf{r}) = |\Psi_{\mathbf{k}}(\mathbf{r})|^2$ and equilibrium spin currents (ESCs) $J_{ij;\mathbf{k}}(\mathbf{r})$ as a function of the twist angle θ (here, $i = x, y, z$ is the polarization direction and $j = x, y$ is the velocity direction). The main results of this Letter are as follows: (1) On varying the twist angle θ (for fixed k_x) $\rho_{k_x}(\mathbf{r})$ and $J_{ij;k_x}(\mathbf{r})$ are shown to have discontinuous derivatives with respect to θ at angles $\{\theta_2(k_x), \theta_3(k_x)\}$ that are close to within of the respective magic angles θ_{2m} and θ_{3m} (obtained by minimization of the bandwidth). Hence, measuring the local density [by scanning tunneling microscopy (STM)] or ESCs (by optospintronic devices [20]) can serve as an excellent tool for determining the magic angles. (2) The symmetry $J_{yx} = -J_{xy}$ and the equalities $J_{xx} = J_{yy} = 0$, valid in single-layer graphene [23], are broken. (3) The relation $\theta_{3m} \approx \sqrt{2}\theta_{2m}$ is extended beyond the chiral limit. (4) Unlike in single or double *untwisted* layer graphene, the ESCs depend on the position $\mathbf{r}$, implying the possible occurrence of spin torque [24,25].

Formalism. Here, we develop the formalism for TBG (an extension for TTG is straightforward). Consider massless two-dimensional (2D) Dirac electrons in TBG lying in the x-y plane with twist angles $\pm\theta/2$ subject to a uniform electric field $\mathbf{E} = E_0\hat{\mathbf{z}}$. We start from the continuous moiré band model [8] wherein there is no valley mixing. The Dirac $\mathbf{K}$ points in adjacent layers 1 and 2 (denoted $\{\mathbf{K}_1, \mathbf{K}_2\}$) are offset by the twisting angle θ [26]. This procedure defines the moiré $\mathbf{Q}$ lattice M_Q shown in Fig. 6(b) of Ref. [8], wherein the *red and blue points*, $\{\mathbf{Q}_1\}$ and $\{\mathbf{Q}_2\}$, denote the $\mathbf{K}$ points in layers 1 and 2, respectively. Occasionally, $\mathbf{Q}$ will denote both. Adjacent $\mathbf{K}$ points of different layers are connected by three vectors $\{\mathbf{q}_j\}$ [see Eq. (5) below]. The θ dependent length of the vectors $|\mathbf{q}_j| = K_D = 2K\sin(\theta/2)$ is the M_Q lattice constant (here, $K = |\mathbf{K}_1| = |\mathbf{K}_2|$ [27]). The Γ point marks the center of the unit cell, and the electron wave number is $\mathbf{k} = (k_x, k_y) \in$ BZ of M_Q. Practically, the number $N_{\mathbf{Q}}$ of $\mathbf{Q}$ points is cutoff within a circle centered at the Γ point, thereby conserving the rotation symmetries specified in Ref. [9]. Explicitly, $N_{\mathbf{Q}_1} = N_{\mathbf{Q}_2} = 50, \Rightarrow N_{\mathbf{Q}} = 100$. We denote by $\boldsymbol{\tau}$ the isospin encoding the two-lattice structure of single-layer graphene, by $\boldsymbol{\eta}$ the pseudospin operator for the two layers and by $\boldsymbol{\sigma}$ the operator for the electron real spin. The pertinent eight-dimensional Hilbert space is then $\boldsymbol{\eta} \otimes \boldsymbol{\sigma} \otimes \boldsymbol{\tau}$. RSOC is introduced as an SU(2) vector potential, $\mathbf{A} = [\boldsymbol{\sigma} \times \hat{\mathbf{z}}]$. In $\mathbf{r}$ space the

Hamiltonian $H = H_0(\mathbf{r}) + H_1$ is

$$H_0(\mathbf{r}) = \eta_0 \otimes [-i\sigma_0\partial_{\mathbf{r}} + \lambda\mathbf{A}]\cdot\boldsymbol{\tau} - \frac{\theta}{2}\eta_z[(-i)\sigma_0\partial_{\mathbf{r}} + \lambda\mathbf{A}]\times\boldsymbol{\tau},$$
$$H_1 = \eta^-\sigma_0 T^\dagger + \eta^+\sigma_0 T. \tag{1}$$

H is the extension of the Hamiltonian introduced in Eq. (1) of Ref. [8], with RSOC included. Here λ, which is proportional to E_0, is the RSOC strength, and T is a 2×2 matrix in $\boldsymbol{\tau}$ space (see below).

We define shifted wave numbers $\mathbf{p}_\eta = \mathbf{k} - \mathbf{Q}_\eta$ ($\eta = 1, 2$ for layers 1,2). The basis eigenfunctions of $H_0(\mathbf{r})$ are $e^{i\mathbf{p}_\eta\cdot\mathbf{r}}v_i(\mathbf{p}_\eta)$, where $\{v_i(\mathbf{p}_\eta)\ (i = 1, 2, \ldots, 8)\}$ are the eight-dimensional eigenvectors of the 8×8 matrix obtained after replacing $-i\partial_{\mathbf{r}} \to \mathbf{p}_\eta$ in Eq. (1). The corresponding energies are $\epsilon_i(\mathbf{p}_\eta)$. Putting together these eight column eigenvectors defines an 8×8 eigenvector matrix $\mathbf{v}(\mathbf{p}_\eta)$. Both $v_i(\mathbf{p}_\eta)$ and $\epsilon_i(\mathbf{p}_\eta)$ are expressible analytically. A Bloch eigenfunction of H (an eight-dimensional vector) is expanded in plane-wave spinors $\{e^{-i\mathbf{Q}_\eta\cdot\mathbf{r}}\mathbf{w}(\mathbf{p}_\eta)\}$ [defined in Eq. (2)] as

$$\Psi_{\mathbf{k}}(\mathbf{r}) = \frac{e^{i\mathbf{k}\cdot\mathbf{r}}}{\sqrt{A}}\sum_{\eta=1}^{2} u_{\eta\mathbf{k}}(\mathbf{r})$$
$$u_{\eta\mathbf{k}}(\mathbf{r}) = \sum_{\mathbf{Q}_\eta\in M_Q} e^{-i\mathbf{Q}_\eta\cdot\mathbf{r}}\underbrace{\left[\sum_{i=1}^{8} a_i(\mathbf{p}_\eta)v_i(\mathbf{p}_\eta)\right]}_{\mathbf{w}(\mathbf{p}_\eta)}. \tag{2}$$

Here, A is the area of a unit cell (moiré hexagon) in position space, and $\{a_i(\mathbf{p}_\eta)\}$ are N (yet unknown) coefficients. The functions $\{u_{\eta\mathbf{k}}(\mathbf{r})\}$ are dimensionless, and periodic on their respective triangular (Bravais) lattices in $\mathbf{r}$ space. The Bloch functions $\{\Psi_{\mathbf{k}}(\mathbf{r})\}$ and the coefficients $\{a_i(\mathbf{p}_\eta)\}$ should carry also a band number n that is occasionally omitted for convenience. Two notational definitions are useful: (1) The 100 8×8 matrices $\{\mathbf{v}(\mathbf{p}_\eta)\}$, are used to form an $N\times N$ block diagonal matrix

$$V \equiv \mathrm{diag}\underbrace{[\mathbf{v}(\mathbf{p}_\eta)]}_{8\times 8}, \quad \mathbf{p}_\eta = \mathbf{k} - \mathbf{Q}_\eta, \quad \mathbf{Q}_\eta \in M_Q. \tag{3}$$

(2) The N unknown coefficients on the right-hand side of Eq. (2) are arranged to form a vector (of N components) $\mathbf{a} \equiv \{a_i(\mathbf{p}_\eta)\}$, where $i = 1, \ldots, 8$.

The eigenvalue equation for the vector $\mathbf{a}$ employs the Bloch representation of the Hamiltonian $\mathcal{H} = V^\dagger H V$ in the presence of RSOC:

$$\mathcal{H}\mathbf{a}_n(\mathbf{k}) = \varepsilon_n(\mathbf{k})\mathbf{a}_n(\mathbf{k}),$$
$$H_{\mathbf{Q},\mathbf{Q}'} = \frac{1}{A}\int e^{-i\mathbf{Q}\cdot\mathbf{r}}H(\mathbf{r})e^{i\mathbf{Q}'\cdot\mathbf{r}}d\mathbf{r}. \tag{4}$$

$H_{\mathbf{Q},\mathbf{Q}'}$ is an 8×8 matrix in $\boldsymbol{\eta}\otimes\boldsymbol{\sigma}\otimes\boldsymbol{\tau}$ space, and $\dim[H] = N\times N$ ($N = N_{\mathbf{Q}}\times 8 = 800$). Explicitly,

$$H = \begin{bmatrix} H^0_{\mathbf{Q}_1,\mathbf{Q}_1} & H^1_{\mathbf{Q}_1,\mathbf{Q}_2} \\ H^{1\dagger}_{\mathbf{Q}_1,\mathbf{Q}_2} & H^0_{\mathbf{Q}_2,\mathbf{Q}_2} \end{bmatrix}, \quad (\mathbf{Q}_1,\mathbf{Q}_2) = 1, 2, \ldots, N_{\mathbf{Q}},$$
$$H_{\mathbf{Q},\mathbf{Q}'} \equiv H^0_{\mathbf{Q},\mathbf{Q}} + H^1_{\mathbf{Q},\mathbf{Q}'},$$
$$H^0_{\mathbf{Q},\mathbf{Q}}(\mathbf{k}) = \eta_0\otimes[\sigma_0\mathbf{p} + \lambda\mathbf{A}]\cdot\boldsymbol{\tau} - \frac{1}{2}\theta\,\zeta_{\mathbf{Q}}\delta_{\mathbf{Q},\mathbf{Q}'}\eta_z\otimes[\sigma_0\mathbf{p} + \lambda\mathbf{A}]\times\boldsymbol{\tau},$$
$$H^1_{\mathbf{Q},\mathbf{Q}'}(\mathbf{k}) = \eta^-\otimes\sigma_0 T^\dagger_{\mathbf{Q},\mathbf{Q}'} + \eta^+\otimes\sigma_0 T_{\mathbf{Q},\mathbf{Q}'},$$
$$T_{\mathbf{Q},\mathbf{Q}'} = \sum_{j=1}^{3}[\delta_{\mathbf{Q}-\mathbf{Q}'}, \mathbf{q}_j + \delta_{\mathbf{Q}'-\mathbf{Q}}, \mathbf{q}_j]T_j,$$
$$\mathbf{q}_j = K_D\left[\cos\frac{(4j-3)\pi}{6}\hat{\mathbf{x}} + \sin\frac{(4j-3)\pi}{6}\hat{\mathbf{y}}\right],$$
$$T_j = w_0\tau_0 + w_1\left[\cos\frac{2\pi(j-1)}{3}\tau_x + \sin\frac{2\pi(j-1)}{3}\tau_y\right], \tag{5}$$

which is the extension of Eq. (A3) in Ref. [8]. As far as the spectrum is concerned, the diagonalization of $H_{\mathbf{Q},\mathbf{Q}'}$ is sufficient. For calculating wave functions, the eigenvectors $\{\mathbf{a}\}$ are required from the solution of the first of Eq. (4), to be used in Eq. (2).

Results for TBG. The spectrum $\{\varepsilon_n(\mathbf{k})\}$ depends on the potential parameters w_0, w_1, θ, λ. It is calculated on the segment

$$\mathbf{k}\in\mathcal{K} \equiv \left[0 \leqslant k_x \leqslant k_D\frac{\sqrt{3}}{2}, k_y = 0\right], \tag{6}$$

joining the Γ and M points in M_Q [28]. The spin observables depend on $\mathbf{k}$ and (unlike the case of untwisted layers) on the position $\mathbf{r} = (x, y)$ in the unit cell (due to the presence of the coupling matrices $\{T_j\}$). We use the following parameters: $K = 15.0533\ (\mathrm{nm})^{-1}$ [5], $w_0 = 77.0371$ meV, $w_1 = 110.053$ meV, $\lambda = 1.0544 \approx 1$ meV [29–31].

Our first task is to find the magic angle θ_{2m}. There are different criteria for its determination, such as vanishing of the Dirac speed, minimal bandwidth, or maximal band gap to higher bands. Ideally, the lowest band at the magic angle is flat, but within a numerical scheme on a system of finite size the situation is less simple. For every twist angle θ, the lowest conduction band $\varepsilon_0(k_x,\theta) > 0$ depends weakly on $k_x\in\mathcal{K}$. Then θ_{2m} may be defined as the twist angle that minimizes the difference

$$d(\theta) \equiv \{\mathrm{Max}[\varepsilon_0(k_x,\theta)] - \mathrm{Min}[\varepsilon_0(k_x,\theta)]\}. \tag{7}$$

Using this criterion, we find the lowest magic angle to be $\theta_{2m} = 1.099^\circ$. The fact that the band is not perfectly flat [so, strictly speaking, different Bloch functions $\{\Psi_{\mathbf{k}}(\mathbf{r})\}$ are *not degenerate*] poses the question of how to interpret the results obtained for different crystal momenta $\mathbf{k}$. Recall that for single-layer graphene [23], where the energy depends solely on k^2, it is possible to integrate the ESC over a constant energy line that is a circle in the $\mathbf{k}$ plane. This integration procedure over a constant energy line is not applicable here, and the results should be analyzed for each $\mathbf{k}$ separately. Fortunately, there are two factors that can ameliorate this obstacle: (1) There is substantial progress in designing momentum-resolved experiments [32–36], and (2) the angles $\{\theta_2(k_x)\}$ at which the ESC displays nonanalyticity are close to θ_{2m} (within 1%). Therefore, for definiteness, in the following we will present our results for the density and the ESC at $\mathbf{r} = \mathbf{0}$ (the center of the direct moiré lattice unit cell), and for fixed $\mathbf{k} = (k_x, k_y) = (0.05, 0)\ (\mathrm{nm})^{-1}\in\mathcal{K}$, Eq. (6). This choice is convenient because, as shown below, somewhat accidentally,

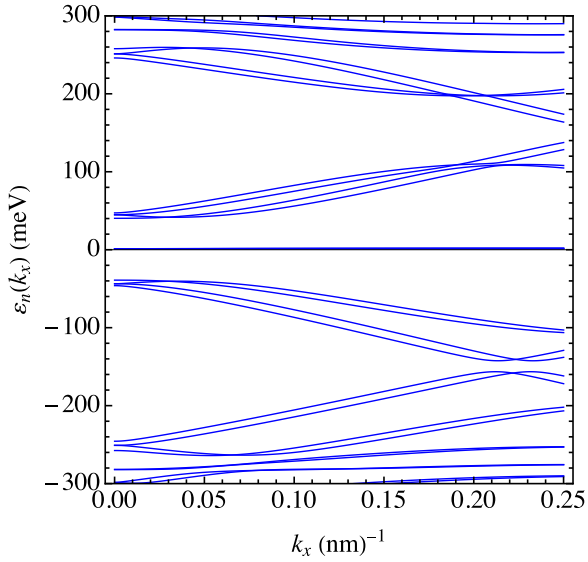

FIG. 1. Low-energy spectrum of TBG at $\theta_{2m} = 1.099^\circ$ for $\mathbf{k} \in \mathcal{K}$ in the presence of RSOC. Here, $\lambda \approx 10$ meV is intentionally enlarged so that the SO splitting is clearly visible. As $\lambda \to 0$, the RSOC splitting shrinks and the level pattern is commensurate with that of Fig. 1(d) in Ref. [8].

at this specific wave number, $\theta_2(k_x = 0.05) = 1.0984^\circ$ just below $\theta_{2m} = 1.0990^\circ$.

The spectrum of several levels above and below the (nearly) flat band is plotted in Fig. 1 for $\lambda \approx 10$ meV (λ is intentionally taken to be much larger than realistic values in order to make the SO splitting visible). Compare with the spectrum for $\lambda = 0$, shown in Fig. 1(d) of Ref. [8].

Density and spin observables in TBG are *local*, and expressed in terms of the Bloch functions $\Psi_{\mathbf{k}}(\mathbf{r})$, Eq. (2), and pertinent operators $\hat{o}$ that are 8×8 matrices in $\boldsymbol{\eta} \otimes \boldsymbol{\sigma} \otimes \boldsymbol{\tau}$ space. The spin and velocity operators are

$$\hat{\mathbf{s}} = \tfrac{1}{2}\hbar\eta_0 \otimes \boldsymbol{\sigma} \otimes \tau_0, \quad \hat{\mathbf{v}} = \eta_0 \otimes \sigma_0 \otimes \boldsymbol{\tau}. \tag{8}$$

The ESC tensor operator is

$$\mathbb{J}_{ij} = \tfrac{1}{2}[\hat{s}_i\hat{v}_j + \hat{v}_j\hat{s}_i] \quad (i = x, y, z, \ \ j = x, y). \tag{9}$$

In the case of m-fold degeneracy (for fixed $\mathbf{k}$), the m degenerate eigenfunctions contribute *incoherently* to the pertinent observable,

$$O_{\mathbf{k}}(\mathbf{r}) = \frac{1}{m}\sum_{n=1}^{m} \Psi^\dagger_{\mathbf{k}n}(\mathbf{r})\hat{o}\Psi_{\mathbf{k}n}(\mathbf{r}). \tag{10}$$

For the charge density, $\hat{o} = \mathbf{1}_{8\times 8}$. Figure 2(a) shows the nonanalyticity at $\theta_2(k_x = 0.05) = 1.0948^\circ$ just below $\theta_{2m} = 1.099^\circ$. For the spin polarization $\mathbf{S}$, $\hat{o} = \hat{s}$, but due to (nontrivial) time reversal invariance the *measured polarization should vanish*. The model of Ref. [4] is uniquely specified for the $\mathbf{K}$ valleys of the two layers from which M_Q is constructed. But time reversal maps $\mathbf{K} \to \mathbf{K}'$ so that each Bloch function $\Psi_{n\mathbf{k}}(\mathbf{r})$ built for the moiré lattice of points $\mathbf{K}$ in Eq. (2) has its Kramers partner $\Psi'_{n\mathbf{k}}(\mathbf{r})$ built for the moiré lattice of points $\mathbf{K}'$. Due to time reversal invariance the sum of the contributions of the two functions to the spin polarization vanishes. In contrast, the ESC is even under time reversal and hence it can

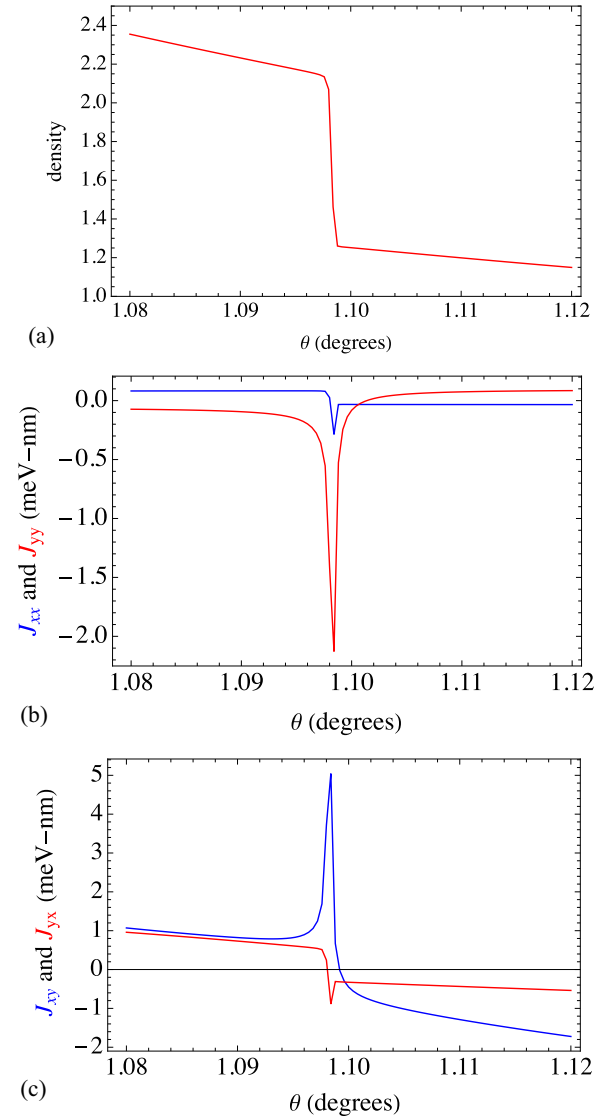

FIG. 2. Local observables of TBG for $\lambda = 1$ meV as a function of θ, displaying singularities at $\theta_2(k_x = 0.05) = 1.0984^\circ$ that are very close to the magic angle $\theta_{2m} = 1.099^\circ$. (a) Dimensionless charge density $A|\Psi_{\mathbf{k}}(\mathbf{0})|^2$ showing a step [a similar step *with the same* $\theta_2(k_x)$ occurs also for $\lambda = 0$]. (b) J_{xx} and J_{yy}. (c) J_{xy} and J_{yx}.

be calculated within the present model wherein the moiré lattice is built solely from the $\mathbf{K}$ points of the two layers. We find that the perpendicular components vanish, $J_{zx} = J_{zy} = 0$, but the planar components are finite. The diagonal planar components J_{xx}, J_{yy} are plotted in Fig. 2(b), while the nondiagonal planar components J_{xy} and J_{yx} are plotted in Fig. 2(c). The singularities occur at the angle $\theta_2(k_x = 0.05) = 1.0984^\circ$. In single-layer graphene [23], $J_{xx} = J_{yy} = 0$ and $J_{xy} = -J_{yx}$. Here, these symmetries are broken.

First chiral limit. References [5,8–10] showed that in the continuous model of TBG there is an approximate antiunitary particle-hole symmetry operator $\mathcal{P}$ that becomes exact in the first chiral limit, $w_0 \to 0$. In this limit, the ESCs vanish (together with the spin polarization), and there are no relevant spin observables. By minimizing the low-

est positive bandwidth it is found that $\theta_{2m-\text{chiral}} = 1.0887^\circ < \theta_{2m} = 1.099^\circ$. The density (not shown in here) is nonanalytic at the (somewhat smaller) angle, namely, $\theta_{2-\text{chiral}}(k_x = 0.05) = 1.0845^\circ < \theta_{2m-\text{chiral}} = 1.0887^\circ$. Thus, the magic angles depend weakly on w_0 (for $w_0 = 77$ meV, $\theta_{2m} = 1.099^\circ$ and for $w_0 = 0$ meV, $\theta_{2m-\text{chiral}} = 1.0887^\circ$).

Twisted three-layer graphene with RSOC. Recently, interest has grown in twisted multilayer graphene [6,37–39]. We shall now briefly address the ESC pattern and the energy spectrum in TTG. As in Ref. [38], we consider a model of alternating-twist three-layer graphene for which the relative twists between two neighboring layers have the same magnitude but alternate in sign (see Fig. 1 therein). As in the case of TBG, we show that as a function of θ, the density and ESC are nonanalytic at the three-layer angle $\theta_3(k_x = 0.05)$. We also extend a remarkable relation suggested (within the chiral limit) in Ref. [38] relating θ_{2m} and θ_{3m}. Calculation of the spectrum and ESC are carried out for the same parameters as for the case of TBG. However, for numerical expediency, we slightly decrease the cutoff used for TBG to include 84 (instead of 100) $\mathbf{Q}$ points, so the Hamiltonian matrix is $N \times N$ with $N = 1008$. Using the notation in Eq. (5), the Hamiltonians of the TTG system are compactly written as

$$H(3) = \begin{bmatrix} H^0_{\mathbf{Q}_1,\mathbf{Q}_1} & H^1_{\mathbf{Q}_1,\mathbf{Q}_2} & 0 \\ H^{1\dagger}_{\mathbf{Q}_1,\mathbf{Q}_2} & H^0_{\mathbf{Q}_2,\mathbf{Q}_2} & H^1_{\mathbf{Q}_2,\mathbf{Q}_1} \\ 0 & H^{1\dagger}_{\mathbf{Q}_2,\mathbf{Q}_1} & H^0_{\mathbf{Q}_1,\mathbf{Q}_1} \end{bmatrix}, \tag{11}$$

where $\mathbf{Q}_1$ and $\mathbf{Q}_2$ run on $1, 2, \ldots, 42$. The technique for extracting spin observables requires a simple extension of the procedure used above for TBG. The Hilbert space is now $\mathbf{\Sigma} \otimes \boldsymbol{\sigma} \otimes \boldsymbol{\tau}$ ($\mathbf{\Sigma}$ is the vector of spin 1 matrices encoding the three layers), so that each Bloch function is now a 12-component plane-wave spinor (after replacing $\boldsymbol{\eta} \to \mathbf{\Sigma}$ in the appropriate expressions). By inspecting the minimum of $d(\theta)$, it is found that the TTG magic angle is $\theta_{3m} = 1.5545^\circ$. In analogy with the TBG system, it is expected that $\theta_3(k_x = 0.05)$ (where the local observables are singular) is very closely below θ_{3m}. This is indeed the case: The charge density for the TTG is shown in Fig. 3(a), while the planar components of the ESC are shown in Figs. 3(b) and 3(c). All the three observables display a singularity at the angle $\theta_3(kx = 0.05) = 1.5536^\circ$. Therefore, the magic angles of the two- and three-layer systems are in excellent accord with the relation derived in Ref. [38] *in the first chiral limit*, namely, the relation $\theta_{3m} \approx \sqrt{2}\theta_{2m}$ is extended to the case $w_0 > 0$. Finally, the spectrum of the TTG system at the magic angle θ_{3m} is shown in Fig. 3(d). It is characterized by a narrow band just above $\varepsilon = 0$ followed by a gap of about 60 meV.

Summary. In this Letter we considered TBG and TTG subject to RSOC. For TBG, using the criterion of minimal bandwidth we determined the magic angle and the spectrum (see Fig. 1), and then analyzed the behavior of charge density and ESC as a function of the twist angle θ. The fact that the band is not ideally flat requires a separate analysis for each crystal momentum k_x. It is shown for $k_x = 0.05$ nm^{-1}, but we checked that for any fixed $k_x \in \mathcal{K}$, the charge density and the ESC are nonanalytic as a function of the twist angle θ as it passes through a certain angle $\theta_2(k_x)$ that is close to the magic angle to within 0.01° (see Fig. 2). Symmetry relations among

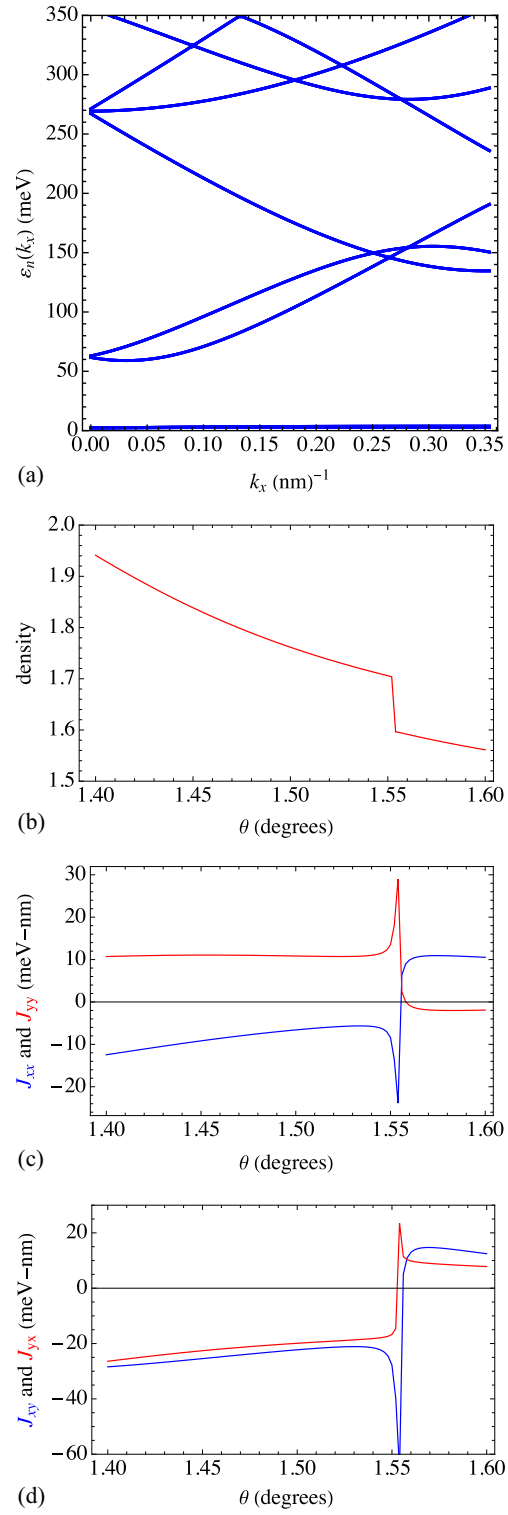

FIG. 3. Results for TTG: Parameters are as in Fig. (2). (a) The spectrum at $\lambda = 0$ for $\mathbf{k} \in \mathcal{K}$ and $\theta_{3m} = 1.5545^\circ$ displays a narrow band close to $\varepsilon = 0$, separated by a large gap of about 60 meV from the next band. For $\lambda = 1$ meV there is a small SO splitting that is invisible on this scale. (b) Dimensionless charge density $A|\Psi_{k_x=0.05}(\mathbf{0})|^2$ vs θ. This pattern is nonanalytic at $\theta_3(k_x = 0.05) = 1.5536^\circ$. Note that $\theta_3(k_x = 0.05) \approx \sqrt{2}\,\theta_2(k_x = 0.05)$. Thus, the relation $\theta_{3m} \approx \sqrt{2}\theta_{2m}$ (derived in Ref. [5] *in the chiral limit*) is extended to the case $w_0 > 0$. (c) and (d) $J_{xx}, J_{yy}, J_{xy}, J_{yx}$ displaying nonanalyticity at $\theta_3(k_x = 0.05) \approx \theta_{3m}$.

ESC components displayed in single-layer graphene [23] and untwisted bilayer graphene are broken in the twisted system. The reason is that in single-layer graphene, the $\mathbf{k}\cdot\mathbf{p}$ expansion around the Dirac points is assumed [23]. The $\mathbf{k}\cdot\mathbf{p}$ model has a continuous rotation symmetry, which is higher than the discrete symmetries of the TBG. This rotational symmetry is broken in TBG. Unlike in Ref. [23], all spin observables depend on the position $\mathbf{r}$, implying the possible occurrence of spin torque [24,25]. The pattern of density and ESC is displayed here for $\mathbf{r}=\mathbf{0}$ but θ_{2m} is independent of $\mathbf{r}$ (within the unit cell).

An analogous study with similar results is shown for TTG, wherein the respective angles $\theta_3(k_x=0.05)$ and θ_{3m} are related to $\theta_2(k_x=0.05)$ and θ_{2m} by a factor $\approx\sqrt{2}$. This extends the relation $\theta_{3m}\approx\sqrt{2}\theta_{2m}$ claimed in Ref. [38] in the chiral limit ($w_0=0$) also for $w_0>0$.

Thus, in addition to the association of magic angles with flat bands, correlated insulating states, unconventional superconductivity, ferromagnetism with an anomalous Hall effect, and distinct Landau level degeneracies, they are also relevant to spin physics. Following the recent developments in the research of monolayer and (untwisted) multilayer graphene spintronics [34,35], we hope our study will stimulate experimental and further theoretical work on the role of magic angles to the spin physics of moiré systems. This expectation is corroborated by the hope that ESCs can be measured using spin- and angle-resolved photoelectron spectroscopy [32–35] and polarized light scattering [36].

Acknowledgments. We are grateful to Rafi Bistritzer, Zhi-Da Song, Pilkyung Moon, Alex Kruchkov, and Ady Stern for useful discussions.

[1] J. M. B. Lopes dos Santos, N. M. R. Peres, and A. H. Castro Neto, Phys. Rev. Lett. **99**, 256802 (2007).
[2] G. Li, G. Li, A. Luican, J. M. B. Lopes dos Santos, A. H. Castro Neto, A. Reina, J. Kong, and E. Y. Andrei, Nat. Phys. **6**, 109 (2010).
[3] P. Moon and M. Koshino, Phys. Rev. B **85**, 195458 (2012); **87**, 205404 (2013); **90**, 155406 (2014).
[4] R. Bistritzer and A. H. MacDonald, Proc. Natl. Acad. Sci. USA **108**, 12233 (2011).
[5] G. Tarnopolsky, A. J. Kruchkov, and A. Vishwanath, Phys. Rev. Lett. **122**, 106405 (2019).
[6] Y. Cao, J. M. Park, K. Watanabe, T. Taniguchi, and P. Jarillo-Herrero, arXiv:2103.12083.
[7] Z. Sun and Y. H. Hu, Matter **2**, 1106 (2020).
[8] Z.-D. Song, B. Lian, N. Regnault, and B. A. Bernevig, Phys. Rev. B **103**, 205414 (2021).
[9] Z. Song, Z. Wang, W. Shi, G. Li, C. Fang, and B. A. Bernevig, Phys. Rev. Lett. **123**, 036401 (2019).
[10] B. A. Bernevig, Z.-D. Song, N. Regnault, and B. Lian, Phys. Rev. B **103**, 205413 (2021).
[11] Y. Cao, V. Fatemi, A. Demir, S. Fang, S. L. Tomarken, J. Y. Luo, J. D. Sanchez-Yamagishi, K. Watanabe, T. Taniguchi, E. Kaxiras *et al.*, Nature (London) **556**, 80 (2018).
[12] Y. Cao, J. Y. Luo, V. Fatemi, S. Fang, J. D. Sanchez-Yamagishi, K. Watanabe, T. Taniguchi, E. Kaxiras, and P. Jarillo-Herrero, Phys. Rev. Lett. **117**, 116804 (2016).
[13] Y. Cao, V. Fatemi, S. Fang, K. Watanabe, T. Taniguchi, E. Kaxiras, and P. Jarillo-Herrero, Nature (London) **556**, 43 (2018).
[14] X. Lu, P. Stepanov, W. Yang, M. Xie, M. A. Aamir, I. Das, C. Urgell, K. Watanabe, T. Taniguchi, G. Zhang *et al.*, Nature (London) **574**, 653-657 (2019).
[15] A. L. Sharpe, E. J. Fox, A. W. Barnard, J. Finney, K. Watanabe, T. Taniguchi, and M. A. Kastner, and D. Goldhaber-Gordon, Science **365**, 605 (2019).
[16] J. H. Pixley and E. Y. Andrei, Science **365**, 543 (2019).
[17] M. Serlin, C. L. Tschirhart, H. Polshyn, Y. Zhang, J. Zhu, K. Watanabe, T. Taniguchi, L. Balents, and A. F. Young, Science **367**, 900 (2020).
[18] T. Stauber, J. Gonzalez, and G. Gomez-Santos, Phys. Rev. B **102**, 081404(R) (2020).
[19] T. M. R. Wolf, O. Zilberberg, G. Blatter, and J. L. Lado, Phys. Rev. Lett. **126**, 056803 (2021).
[20] J. F. Sierra, J. Fabian, R. K. Kawakami, S. Roche, and S. O. Valenzuela, Nat. Nanotechnol. **16**, 856 (2021).
[21] A. Uri, S. Grover, Y. Cao, J. A. Crosse, K. Bagani, D. Rodan-Legrain, Y. Myasoedov, K. Watanabe, T. Taniguchi, P. Moon, M. Koshino, P. Jarillo-Herrero, and E. Zeldov, Nature (London) **581**, 47 (2020).
[22] E. I. Rashba, Sov. Phys. Solid State **2**, 1109 (1960); Y. A. Bychkov and E. I. Rashba, JETP Lett. **39**, 78 (1984); H. A. Engel, E. I. Rashba, and B. I. Halperin, arXiv:cond-mat/0603306.
[23] H. Zhang, Z. Ma, and J. F. Liu, Sci. Rep. **4**, 6464 (2015).
[24] J. Shi, P. Zhang, D. Xiao, and Q. Niu, Phys. Rev. Lett. **96**, 076604 (2006).
[25] Y. Avishai and Y. B. Band, Phys. Rev. B **103**, 134445 (2021).
[26] See Ref. [8], Fig. 7(a).
[27] See Ref. [8], Fig. 7(b).
[28] See Ref. [8], Fig. 1(b).
[29] M. Gmitra, S. Konschuh, C. Ertler, C. Ambrosch-Draxl, and J. Fabian, Phys. Rev. B **80**, 235431 (2009).
[30] S. Konschuh, M. Gmitra, and J. Fabian, Phys. Rev. B **82**, 245412 (2010).
[31] M. Gmitra and J. Fabian, Phys. Rev. B **92**, 155403 (2015).
[32] C. Tusche, A. Krasyuk, and J. Kirschner, Ultramicroscopy **159**, 520 (2015).
[33] M. Ünzelmann, H. Bentmann, T. Figgemeier, P. Eck, J. N. Neu, B. Geldiyev, F. Diekmann, S. Rohlf, J. Buck, M. Hoesch, M. Kalläne, K. Rossnagel, R. Thomale, T. Siegrist, G. Sangiovanni, D. Di Sante, and F. Reinert, Nat. Commun. **12**, 3650 (2021).
[34] A. Avsar, H. Ochoa, F. Guinea, B. Özyilmaz, B. J. van Wees, and I. J. Vera-Marun, Rev. Mod. Phys. **92**, 021003 (2020).
[35] K. Zollner and J. Fabian, Phys. Rev. B **104**, 075126 (2021).
[36] J. Wang, B.-F. Zhu, and R.-B. Liu, Phys. Rev. Lett. **100**, 086603 (2008).
[37] J. M. Park, Y. Cao, K. Watanabe, T. Taniguchi, and P. Jarillo-Herrero, Nature (London) **595**, 526 (2021).
[38] Z. Hao, A. M. Zimmerman, P. Ledwith, E. Khalaf, D. H. Najafabadi, K. Watanabe, T. Taniguchi, A. Vishwanath, and P. Kim, Science **371**, 1133 (2021).
[39] V. T. Phong, P. A. Pantaléon, T. Cea, and F. Guinea, arXiv:2106.14911.